A&A 664, A153 (2022)
https://doi.org/10.1051/0004-6361/202243409

Astronomy & Astrophysics

Extremely high spectral resolution measurements of the 450 μm atmospheric window at Chajnantor with APEX⋆,⋆⋆

J. R. Pardo[1,5], C. De Breuck[2], D. Muders[3], J. González[2], F. M. Montenegro-Montes[4], J. P. Pérez-Beaupuits[4], J. Cernicharo[1], C. Prigent[5], E. Serabyn[6], T. Mroczkowski[2], and N. Phillips[2]

[1] Consejo Superior de Investigaciones Cientifícas, Instituto de Física Fundamental, Serrano 123, 28006 Madrid, Spain
e-mail: jr.pardo@csic.es
[2] European Southern Observatory, Karl-Schwarzschild-Str. 2, 85748 Garching, Germany
[3] Max-Planck-Institut für Radioastronomie, Auf dem Hügel 69, 53121 Bonn, Germany
[4] European Southern Observatory, Alonso de Córdova 3107, Vitacura Casilla 7630355, Santiago, Chile
[5] Centre National de la Recherche Scientifique, Observatoire de Paris, Laboratoire d'Études du Rayonnement et la Matière en Astrophysique, 77 Avenue Denfert Rochereau, 75014 Paris, France
[6] Jet Propulsion Laboratory, California Institute of Technology, 4800 Oak Grove Drive, Pasadena, CA 91109, USA

Received 23 February 2022 / Accepted 17 May 2022

ABSTRACT

Ground-based telescopes observing at millimeter (mm) and submillimeter (submm) wavelengths have to deal with a line-rich and highly variable atmospheric spectrum, both in space and time. Models of this spectrum play an important role in planning observations that are appropriate for the weather conditions and also calibrating those observations. Through magnetic dipolar (M1) rotational transitions and electric dipolar (E1) transitions O_2 and H_2O, respectively, dominate the atmospheric opacity in this part of the electromagnetic spectrum. Although O_2 lines, and more generally the so-called dry opacity, are relatively constant, the absorption related to H_2O can change by several orders of magnitude leading from a totally opaque atmosphere near sea level with high H_2O columns to frequency windows with good transmission from high and dry mountain sites. Other minor atmospheric gases, such as O_3 and N_2O among others, are present in the atmospheric spectrum which also includes nonresonant collision-induced absorption due to several mechanisms. The aim of our research is to improve the characterization of the mm/submm atmospheric spectrum using very stable heterodyne receivers with excellent sideband separation and extremely high (kHz) spectral resolutions at the 5000 m altitude Chajnantor site in northern Chile. This last aspect (spectral resolution) is the main improvement (by more than three orders of magnitude) in the presented data with respect to our previous work conducted ∼20 yr ago from Mauna Kea in Hawai'i. These new measurements have enabled us to identify slight modifications needed in the Atmospheric Transmission at Microwaves (ATM) model to better take into account minor constituent vertical profiles, include a few missing lines, and adjust some high-energy O_3 line frequencies. After these updates, the ATM model is highly consistent with all data sets presented in this work (within ∼2% at 1 GHz resolution).

Key words. atmospheric effects – techniques: spectroscopic – molecular data – line: profiles – opacity

1. Introduction

The detailed knowledge of the atmospheric spectrum in the millimeter (mm) and submillimeter (submm) regions of the electromagnetic spectrum, typically from ∼30 GHz to ∼1.0–1.6 THz, has been crucial for developing new science in astrophysics through observations of the Molecular Universe. The vast majority of polar molecules in space have been discovered through observations of some of their rotational transitions in that frequency range. Combining observations from more than one line of a given molecule has also enabled the study of the physical conditions of a wide range of astronomical objects, such as cold dark clouds, star-forming regions, evolved stars, galaxies, and many others.

Since the beginning of molecular astrophysics, efforts have been made to measure, characterize, and model atmospheric effects in the frequencies concerned. One of earliest works was conducted in the 1970s from Tenerife at ∼2400 m above sea level by Hills et al. (1978). Those measurements were the first to show the presence of submm atmospheric windows at high and dry mountain sites, motivating the construction of submm observatories that began operations about one decade later in Mauna Kea (Hawai'i). Site testing for ground-based submm observatories and field spectroscopy experiments continued over the years in Mauna Kea, in the Atacama desert in Chile, and in the South Pole, leading to several relevant publications, such as Matsushita et al. (1999), Paine et al. (2000), Pardo et al. (2001a), Chamberlin et al. (2003), and Mlawer et al. (2019), based on data from broadband (several hundred gigahertz) Fourier transform spectrometers (FTSs). The frequency resolution in these experiments ranged from ∼0.2 to 10 GHz, which allows the study of the very broad features of the spectrum related to H_2O and O_2 lines, as well as nonresonant wet and dry collision-induced absorption (CIA). However, obtaining the details of the large number of narrow absorption features present in the atmospheric spectrum requires much finer spectral resolutions.

⋆ Recalibrated data are only available at the CDS via anonymous ftp to cdsarc.u-strasbg.fr (130.79.128.5) or via http://cdsarc.u-strasbg.fr/viz-bin/cat/J/A+A/664/A153

⋆⋆ This publication is based on data acquired with the Atacama Pathfinder Experiment (APEX) under programme ID 105.2084. APEX is a collaboration between the Max-Planck-Institut für Radioastronomie, the European Southern Observatory, and the Onsala Space Observatory.

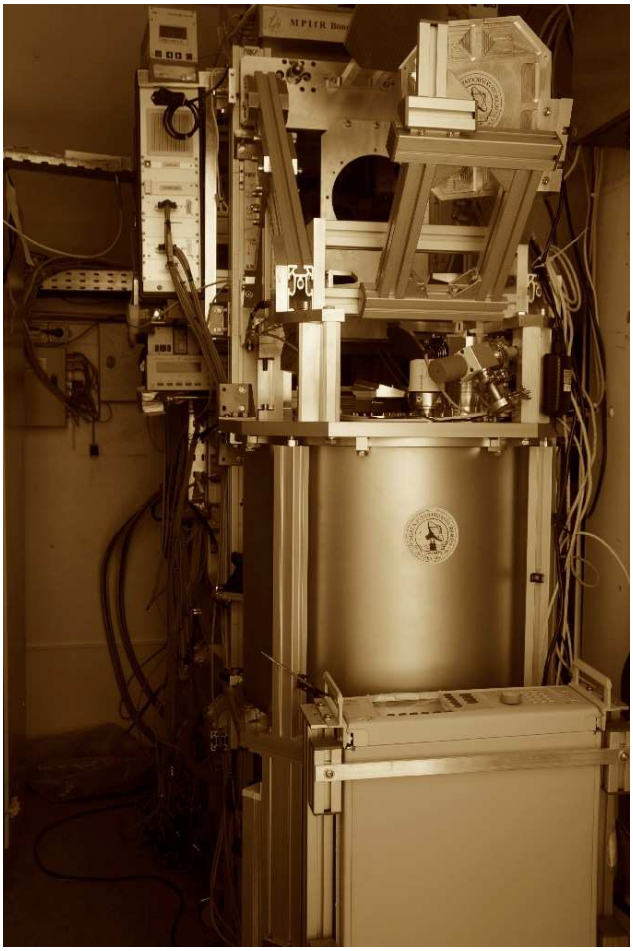

Fig. 1. SEPIA is a single-pixel heterodyne receiver with a cryostat that can accommodate three receiver cartridges: SEPIA660, used in this work, plus SEPIA345 (272–376 GHz) and SEPIA180 (159–211 GHz).

The meteorological observations from satellites in the microwave domain are currently limited to below 190 GHz. The upcoming European Organisation for the Exploitation of Meteorological Satellites (EUMETSAT) Polar System-Second Generation (MetOp-SG) will carry an instrument, the Ice Cloud Imager (ICI), with frequencies up to 664 GHz (Klein et al. 2016). The primary objective of the ICI is to improve the characterization of the ice clouds. Quantitative exploitation of the ICI observations requires a thorough understanding of the atmospheric gas absorption in this frequency range, which the weather prediction community has not yet investigated. The detection and quantification of the thin ice clouds with ICI will be particularly sensitive to the accuracy of the gas absorption model (Mattioli et al. 2019).

The aim of the present work is therefore to make a step forward in the characterization of the atmospheric submm spectrum as seen from high and dry mountain-top sites, especially targeting weaker and narrower features than in previous studies. In addition, the high frequency resolution should help in checking details about the integrated column of minor atmospheric gases and also their vertical distribution. Finally, the wet and dry CIA can be revisited with new data from a site (Chajnantor) where the dry absorption should suffer from much smaller fluctuations than the wet one, as was the case for Mauna Kea.

To achieve these goals, we use the heterodyne receivers installed at the Atacama Pathfinder Experiment (APEX) telescope, in particular in this paper the Swedish ESO PI Instrument at APEX (SEPIA, see Fig. 1, Sect. 3 and Belitsky et al. 2018), which covers the 450 µm atmospheric window (SEPIA660 for its central frequency of ~660 GHz). Compared to our previous work at Mauna Kea with a broadband FTS (Pardo et al. 2001a), this study uses an extremely fine spectral resolution of a few tens of kHz achieved by the fourth-generation dual-input Fast Fourier Transform Spectrometer (dFFTS4G) but with a narrower instantaneous band (typically ~8 GHz); see Klein et al. (2012). The narrow spectral band requires many individual frequency tunings to cover the full atmospheric window, which implies stitching together many individual scans that, for consistency, need both a stable atmosphere and instrumental behavior. Until now, this last issue has prevented the kind of studies that we present here. Atmospheric scans using heterodyne receivers usually suffer from strong baseline ripples and inconsistencies from one tuning to another, meaning that only the differential position or frequency switch scans on astronomical sources are exploitable. The stability of the SEPIA660 receiver system in total power measurements (with Allan times of between 5 and 10 seconds) and its high sideband rejection ratio (typically >20 dB) have improved this situation (see SEPIA660[1] and Hesper et al. 2017), and it is now possible to acquire reasonably clean atmospheric spectra at kilohertz resolution.

This paper is the first in a series, and as such will mainly focus on the 'proof of concept' of APEX/SEPIA/dFFTS4G which is designed to measure the Earth's atmospheric spectrum in detail across the mm and submm ranges of the electromagnetic spectrum. The reference atmospheric radiative transfer model used in this work, introduced in Sect. 2, is Atmospheric Transmission at Microwaves (ATM), which is currently used in operations by the Atacama Large Millimeter/submillimeter Array (ALMA) software as part of the Telescope Calibration subsystem, which is made available by the ALMA Open Source Software Project through[2]. The observations are presented in Sect. 3, together with a description of the SEPIA660 receiver. The calibration scheme is described in Sect. 4. The first good-quality results, obtained during a very stable observing run on December 6, 2020, are presented in Sect. 5. Model calculations to reproduce the observations are presented and discussed in Sect. 6. Finally, we provide a summary of our findings and conclusions in Sect. 7.

2. Atmospheric radiative-transfer model

The ATM model includes the spectroscopy and reference vertical profiles for all relevant molecular species contributing to the mm and submm atmospheric spectrum as seen from ground-based observatories, along with empirical and theoretical descriptions of the CIA mechanisms such as N_2-N_2 + O_2-O_2 + O_2-N_2 (dry CIA), H_2O-N_2 + H_2-O_2 ("foreign" wet CIA), and H_2O-H_2O ("self" wet CIA). The data presented and analyzed in this paper belong to a larger study for which the validation and upgrades of the ATM model for the Chajnantor site is one of the goals. ATM is described in detail in Pardo et al. (2001b).

3. Observations

The observations presented in this paper were carried out on December 6, 2020, between 10:43:33 and 13:54:30 UTC using

[1] https://www.apex-telescope.org/ns/instruments/sepia/sepia660

[2] https://bitbucket.alma.cl/projects/ASW/repos/telcal/browse/TelCalResults/Libraries/ATM

the SEPIA660 receiver, which is a dual-polarization sideband separating (2SB) receiver installed and commissioned during the second half of 2018. It replaces the previous double side band (DSB) receiver built to the specifications of ALMA Band 9 (602–720 GHz), based on a pre-production ALMA Band 9 receiver cartridge. SEPIA660 covers the Radio Frequency (RF) range 578–738 GHz (an extended range of 574–742 GHz can be sampled, but with unspecified performance) thanks to a re-programming of the Yttrium Iron Garnet (YIG) tuned oscillator. A complete technical description is given by Hesper et al. (2017). Thanks to careful selection of optimally matched junctions, the sideband rejection ratio has been measured to be as good as 25 dB or better over most of the RF and Intermediate Frequency (IF) range. The receiver simultaneously covers the IF range from −12 to −4 GHz and from 4 to 12 GHz in both polarizations. The receiver temperature of the SEPIA660 frequency channel is below 350 K at all frequencies within the RF band, and below 250 K in the frequency range 600–700 GHz. In Klein et al. (2012), the receiver IF outputs were analyzed with the dFFTS4G spectrometer, which features a total of 16 bands of 4 GHz with 65 536 spectral channels each, thus delivering ∼61 kHz resolution. Each 4–12 GHz IF signal was sampled with two bands with some frequency overlap.

Weather conditions were quite dry with a precipitable water vapor column (PWVC) below 0.5 mm according to the estimations from the water vapor radiometer (WVR) installed at the APEX telescope. This parameter and several others from the weather station (pressure, temperature, wind speed, and relative humidity at ground level) were stored in a log file together with other parameters related to the observations (azimuth, elevation, receiver tuning). This allows us to obtain an overall view of the conditions during our experiment, which are very important in the analysis of the results. For each observing frequency, we performed a hot, cold, and sky calibration with an integration time of 10 s, where the hot and cold loads are from the standard APEX Nasmyth A calibration unit (see Sect. 4). This sequence was repeated for five airmasses (1.0, 1.25, 1.5, 1.75 and 2.0) at a fixed azimuth of 180° (south), and the entire procedure then restarted for the next tuning frequency. We used a total of 24 tunings with central frequencies from 580 to 736 GHz in steps of 7 GHz. Due to the limited range of the local oscillator, the four lowest frequency tunings were set up with the tuning requested frequency in the lower sideband, while for all other 20 tunings it was placed in the upper sideband.

4. Calibration

The final products of the observations presented in this paper are atmospheric spectra in terms of what we refer to here as equivalent blackbody temperature at each frequency, $T_{\rm EBB}(\nu)$. If $F_{\rm atm}(\nu)$ is the calibrated atmospheric flux at frequency ν, $T_{\rm EBB}(\nu)$ is derived from: $F_{\rm atm}(\nu) = B[T_{\rm EBB}(\nu)]$ with B being the blackbody function. In order to get $F_{\rm atm}(\nu)$ or $T_{\rm EBB}(\nu)$ free from the optical-electrical functions of the observing system, two black bodies at different temperatures are observed with the receiver (Ulich & Haas 1976; Ulich 1980). These black bodies are implemented using a microwave absorber material, one at the receiver cabin temperature ($T_{\rm hot}$), and one at a temperature near that of liquid N_2 at 5100 m altitude (≈73 K). The second absorber is installed in a small dewar and connected to a closed cycle cryocooler. Its radiation is observed through a dewar window which exhibits frequency-dependent transmission coefficients. We measured these coefficients by comparing calibrations with this cold load against those using a liquid N_2 absorber. The deviation from a perfect coupling is modeled as a spillover $\eta(\nu)$ from surfaces at cabin temperature leading to an effective cold absorber temperature of

$$\mathrm{T}_{\rm cold,effective}(\nu) = \mathrm{T}_{\rm cold,physical} \cdot (1 - \eta_{\rm cal}(\nu)) + \mathrm{T}_{\rm hot,physical} \cdot \eta_{\rm cal}(\nu), \quad (1)$$

which is somewhat higher than the measured physical temperature. The spillover in the 660 GHz band is estimated using the following linear fit against frequency (D. Muders, priv. comm.):

$$\eta_{\rm cal,660\ GHz\ band}(\nu) = 1.903 \times 10^{-4} \cdot \nu[\mathrm{GHz}] - 5.083 \times 10^{-2}. \quad (2)$$

This fit was obtained using the early DSB version of the Band 9 receiver, which was installed in 2016. At the time, there were some differences between the two polarizations, but as they were rather small, it was decided to use an average spillover number. This leads to an uncertainty of $\eta_{\rm cal,660\ GHz\ band}$ of the order 0.01 which might contribute to the calibration offset discussed later in this section. In order to obtain the $T_{\rm EBB}(\nu)$ spectra, we modified the APEX Calibrator software (Polehampton et al. 2019) to compute this quantity and write it out in CLASS format (Pety 2018).

4.1. Water vapor retrieval

The main problem that we find with the data is that the sky $\mathrm{T}_{\rm EBB}$ at frequencies with very high opacity – where it should be very close to the temperature of the bottom atmospheric layer – has an unrealistic offset towards lower temperatures (see the second panel on Fig. 3). We do not have a convincing explanation for this calibration issue but it is clear that it should be corrected before continuing our analysis. At the same time, the intervention should be as minimal as possible.

4.1.1. Total precipitable water vapor column

The first step is to retrieve the PWVC from the data in some way that does not depend on the calibration issue. To do so, we found that the best strategy consists in using the ortho-H_2O ($J_{Ka,Kb}$ = $5_{3,2}$–$4_{4,1}$) line with central frequency at 620 700.807 MHz. The upper level of this transition lies at 697.9 K and its quantum line strength is 0.1256. These parameters make this line quite sensitive to the PWVC at the site conditions. To avoid the problem of the calibration offset mentioned above, we can use the differential $\mathrm{T}_{\rm EBB}$ between the most extreme 2.0 and 1.0 airmasses and compare it to the ATM model simulations, assuming the offset does not depend on airmass. By doing so (see Fig. 2), it is clear that the PWVC, at least when the skydip around 620 GHz was done, is 0.325 mm, which is in very good agreement (within <0.005 mm) with the value from WVRs stored in the log file (see Fig. 3).

4.1.2. Water vapor vertical distribution

The geometry of the observations prevents retrieval of the fine details of the water vapor vertical distribution. However, if we simply assume that it is distributed as exponentially decreasing with height, which is the default assumption in the ATM model, the technique of the differential $\mathrm{T}_{\rm EBB}$ can also provide good estimations. Figure 2 shows three curves for PWVC = 0.325 mm, corresponding to three different values of the scale height in the water vapor vertical distribution. The black curve (scale

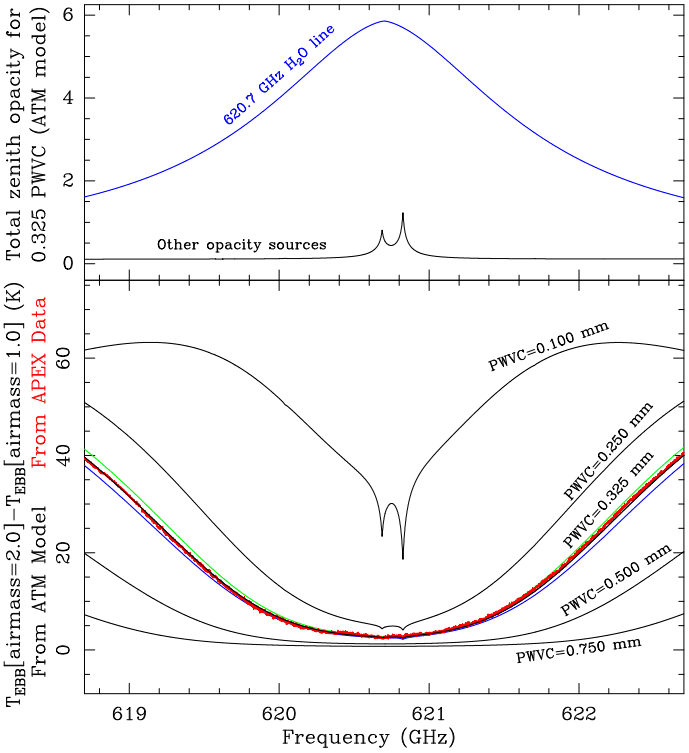

Fig. 2. Retrieval of the reference PWVC during our APEX-SEPIA660 atmospheric observations on December 6, 2020 using the ortho-H_2O $J_{Ka,Kb}$ = $5_{3,2}$–$4_{4,1}$ line at 620.7 GHz. The atmospheric opacity around 620.7 GHz is dominated by that line, meaning that the atmospheric differential T_{EBB} for two airmasses (black curves using the ATM model) provides a way of retrieving the PWVC independently from other parameters in the model and/or calibration issues that are not dependent on the airmass. For a discussion of the green and blue curves for PWVC = 0.325 mm; see Sect. 4.1.2.

height = 2.5 km) provides the best fit to the data. The other two curves correspond to 3.0 km (green) and 2.0 km (blue). In the latter two cases, the differences with respect to the data at ∼1.5 GHz from the line center reach a few Kelvin, whereas the fit is almost perfect for 2.5 km. Therefore, this value was assumed for the ATM simulations throughout this paper.

4.2. Recalibration

Once the PWVC retrieval has produced a consistent result, we have to correct the data for the above mentioned offset. We decided to focus on those frequencies where the atmospheric opacity is expected to be larger than 8.0 at 2.0 airmasses, that is, around 573.0, 620.7, and 740.0 GHz. Even in the very dry conditions experienced during the observations, the ATM model shows that the measured T_{EBB} should be within 2 K of the physical temperature of the bottom atmospheric layer. We therefore applied a very simple recalibration consisting in shifting the 2.0 airmass spectrum so that it matches the ATM model calculations at the above-mentioned three frequencies, and we applied the same shift to the spectra at the four other airmasses (see the third panel of Fig. 3). This means that our re-calibration consists of a global shift and not of a re-scaling. Our assumption is that if our later analysis is consistent, then this re-calibration should be acceptable. If the recalibration were incorrect, inconsistencies should become apparent in the analysis.

5. Results

In order to improve the presentation of the figures and to keep the size of the online files manageable, we applied an eight-channel smoothing to the spectra displayed throughout this paper and in the online material, achieving a final resolution of 489 kHz. The fully calibrated spectra are shown in the second panel of Fig. 3 in terms of T_{EBB} versus frequency following the calibration scheme described in the previous section. All scans for each one of the individual airmasses (1.0, 1.25, 1.5, 1.75 and 2.0) are simply stitched together and plotted as black curves in that panel. As the atmospheric conditions change very smoothly during the observations, and as the system is very stable, the data do not show big discontinuities, although small ones are noticeable towards the high-frequency end, corresponding to the moment of sunrise when the PWVC shows larger fluctuations (see the top panel of Fig. 3). The third panel of Fig. 3 shows the recalibrated data according to the procedure described in the previous section. In order to better see some of the many weaker lines present in the data, thanks to the great stability of the receiver and the low noise of the spectra, Fig. 4 shows zooms onto some selected frequency intervals (labeled 1 to 5) which are highlighted in yellow in Fig. 3. The detection of those weak features and their comparison with model predictions was one of the goals of this study. The following subsections describe the different spectral features and the species responsible for them.

5.1. Water vapor and molecular oxygen

This particular "window" of the atmospheric spectrum is located between two strong water vapor lines: $J_{Ka,Kb} = 1_{1,0}$–$1_{0,1}$ of ortho-H_2O at 556 936.002 MHz (the upper energy level of this transition is E_{up} = 26.7 K, and its quantum line strength S_{ul} = 1.5008) and $J_{Ka,Kb} = 2_{1,1}$–$2_{0,2}$ of para-H_2O at 752 033.227 MHz (E_{up} = 136.9 K, S_{ul} = 2.0709). Even for a very high and dry site such as Chajnantor, these two lines are completely opaque around their central frequencies and they determine the limits of the so-called 450 µm atmospheric window. The minimum in atmospheric opacity is in fact reached near 664 GHz (452 µm in wavelength). We see in the data a general increase in the atmospheric brightness temperature, and therefore the opacity, in both directions from that frequency because of the wings of the two strong water lines mentioned above. This increase is not smooth because of the presence of a multitude of much narrower minor atmospheric gas transitions (see below) and also the strong but stable $^{16}O_2$ $N_J = 5_4$–3_3 line centered at 715 392.889 MHz, which strongly affects the higher frequency end of this window.

Two additional and very important H_2O lines are present in the spectra as they are very sensitive to the PWVC and are therefore crucial in the analysis of these data. The first one at 620 700.807 MHz is mentioned in Sect. 4.1 and used for a relatively precise PWVC retrieval. The other important line corresponds to $J_{Ka,Kb} = 1_{1,0}$–$1_{0,1}$ ortho-H_2O in its ν_2 = 1 vibrational state at 657 968.628 MHz, which is the lowest energy line lying in this state, and is the equivalent of the strong 556 936.002 MHz ortho-H_2O line mentioned above. Because the first bending ν_2 mode of H_2O lies at 2322.92 K, this spectral feature appears much weaker than the above-mentioned 620.7 GHz H_2O line (a few Kelvin in brightness from the lowest T_{EBB} level in this atmospheric window) and its use for PWVC retrieval purposes is somewhat complicated because of ozone lines (see below).

The $J_{Ka,Kb} = 2_{1,1}$–$2_{0,2}$ line of HDO – corresponding to the strongest (μ_b) component of the dipole moment – is detected at 599 926.76 MHz. The zoom onto the data in panel 1 of Fig. 4

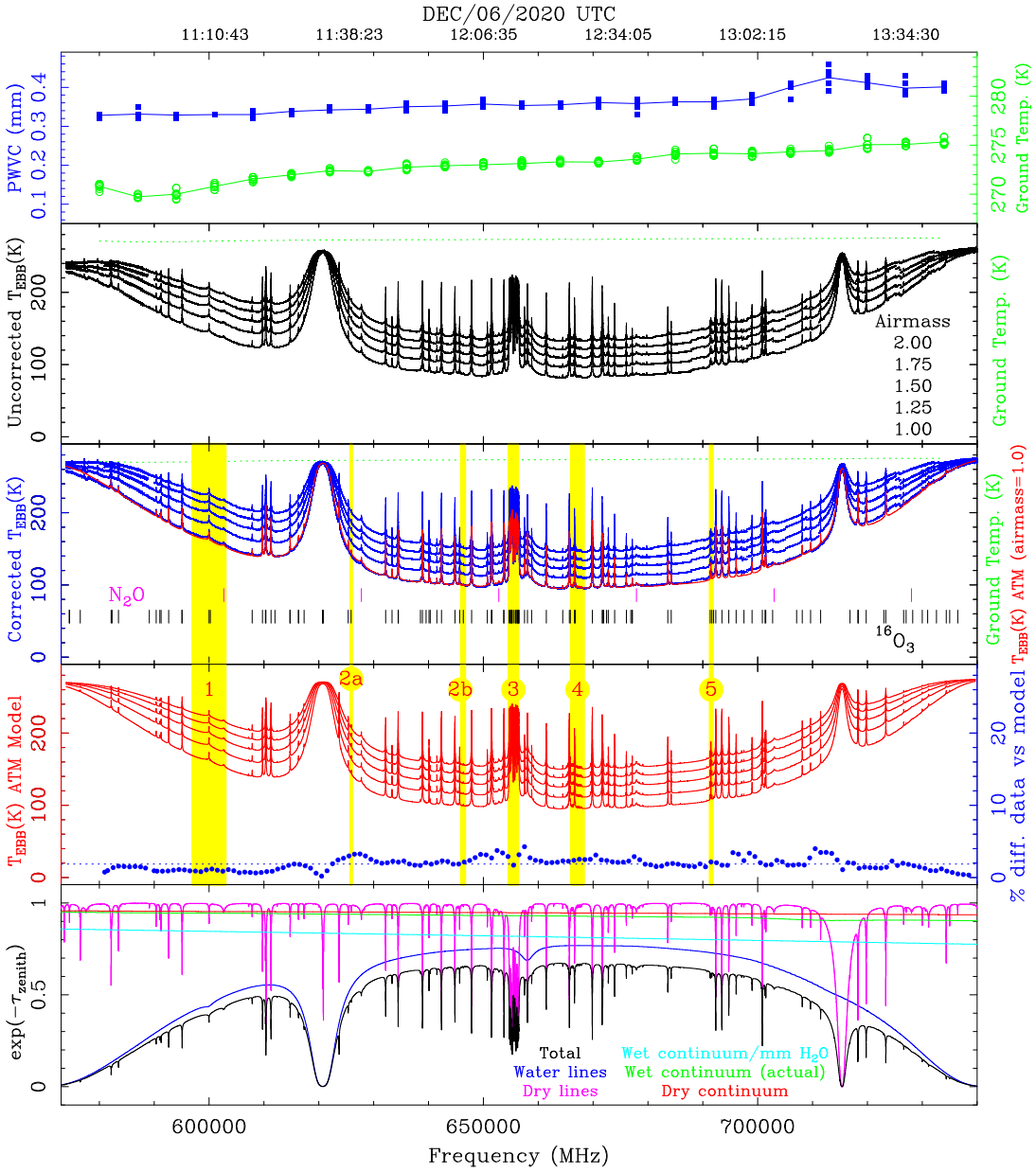

Fig. 3. APEX Atmospheric observing run carried out on December 6, 2020. The panels *from top to bottom* show: atmospheric parameters from the observing log (blue and green); uncorrected spectra from the observations CLASS file (black); corrected spectra (blue, see text) plus ATM model prediction for airmass = 1.0 (red) and line positions for N_2O and O_3; ATM model simulations (red) and data vs model residuals according to Eq. (3) (blue dots, smoothed to 1 GHz); and atmospheric opacity breakdown according to those model results (several colors in the *bottom panel*). Zooms on selected frequency ranges, highlighted in yellow, are displayed in Fig. 4.

shows the line as measured with a narrower $^{16}O_3$ line on top of it. The HDO line is a weak feature of several GHz in width that could be mistaken with a baseline feature unless we compare with the model without HDO.

The $H_2^{17}O$ and $H_2^{18}O$ counterparts of the 620.7 GHz $H_2^{16}O$ line, with the same quantum numbers, $J_{Ka,Kb} = 5_{3,2}$–$4_{4,1}$, are also present in the data but are very difficult to see. The frequency of the ^{17}O substitution is 658 506.157 MHz, which is very close to the stronger 657.97 GHz H_2O line in its first vibrationally excited state. Both lines are mixed, although the last one is clearly dominant as the observed peak lies at its central frequency. We also looked for the ^{18}O counterpart that should be present at 692 079.140 MHz. However, the weakness and width of this line makes it impossible to disentangle in the data.

5.2. Ozone

The most abundant isotopolog of ozone ($^{16}O_3$) is the next most important molecule in this spectral region, exhibiting several tens of narrow lines that emerge with intensities of up to several tens of Kelvin above the broader spectral shape. The central frequencies of these $^{16}O_3$ transitions are marked on the central panel of Fig. 3. An interesting cluster of O_3 lines appears around 656 GHz near (and blended with) the above-mentioned 658 GHz rotational line of water in its $\nu_2 = 1$ vibrational state.

The lowest-lying (bending) vibrationally excited mode of $^{16}O_3$ ($\nu_2 = 1$) at an excitation temperature of 1009.5 K has a population relative to the ground vibrational state that would result in lines reaching a few Kelvin above the broader spectral shape, easily visible in our data (see panel 4 of Fig. 4).

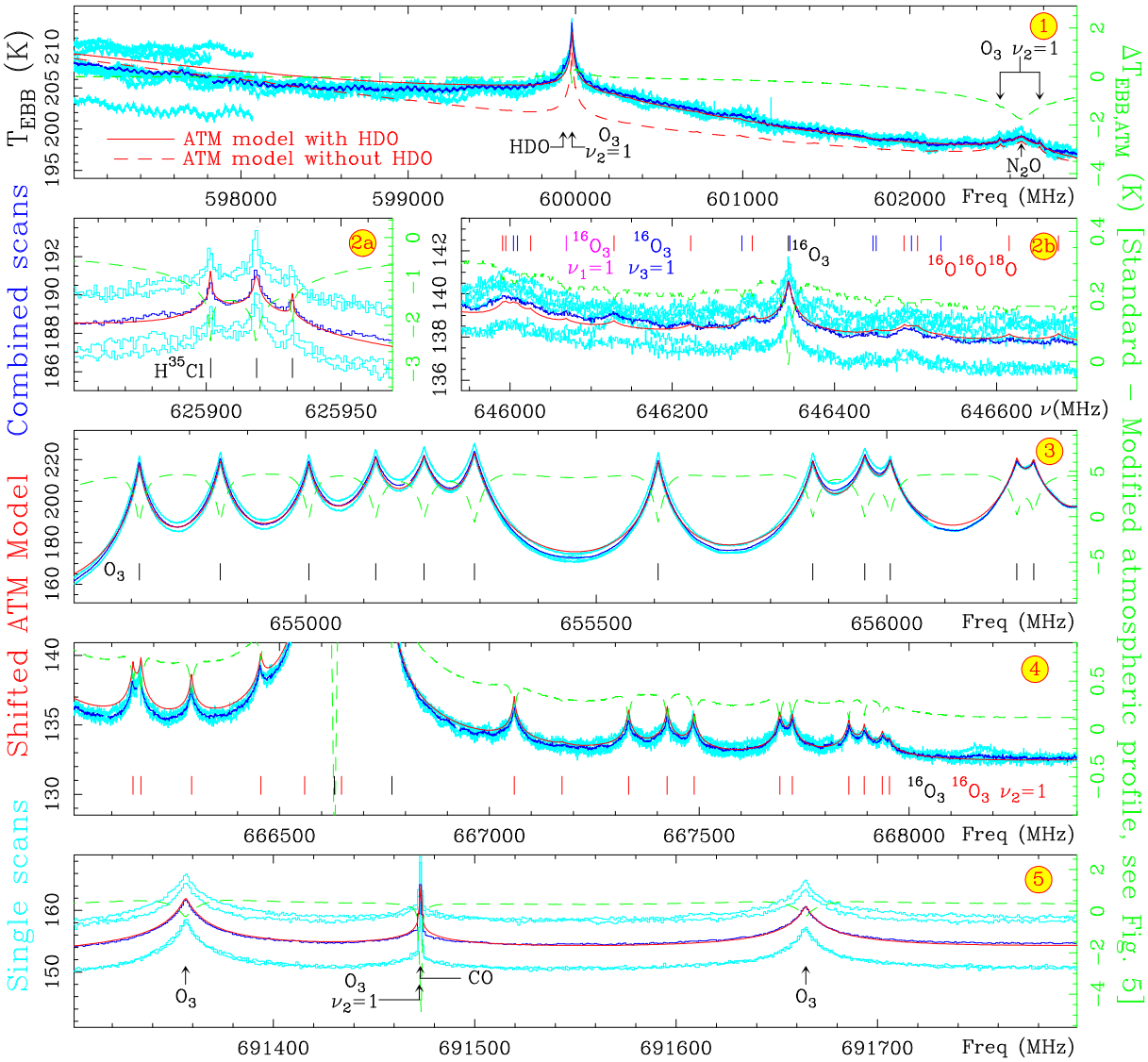

Fig. 4. Zoom onto airmass = 2.0 data showing final combined scans (dark blue) and model predictions (red) in selected frequency ranges. All individual scans are also shown (light blue) and line identifications are also provided. The dashed green lines (with scales on the *right of each panel*) show the ΔT_{EBB} resulting from ATM model simulations with the standard and modified vertical profiles shown in Fig. 5. The data are shown before the recalibration described in Sect. 4.2 because we wanted to show the individual raw scans. Therefore, in this figure it is the ATM model results that have been shifted to match the observed level before recalibration. The different panels are discussed in the text.

Other ozone forms are beyond the limit of detection. For example, some isotopic substitutions of O_3 and its ν_1 = 1 and ν_3 = 1 vibrational states (with excitation temperatures above 1500 K) are expected to display rotational lines of about 0.2–1.0 K above the emission level provided by more abundant species. This intensity is similar to the noise level and/or systemic features seen in our data. Nevertheless, panel 2b of Fig. 4 shows a possible match between very weak features in the observed spectrum and simulated lines from those O_3 vibrationally excited modes.

5.3. Nitrous oxide

The linear molecule N_2O has six of its rotational transitions present in the data, from J = 24–23 up to J = 29–28. With respect to $^{16}O_3$, N_2O lines appear weaker (a less abundant trace gas in the atmosphere) and wider (larger relative abundance at lower altitudes). In fact, the Tropical U.S. Standard Atmosphere (COESA 1976) vertical profile for N_2O in the ATM model has been modified below 30 km (see Fig. 5) in order to get a good match to the observed lines. The central frequencies of these N_2O lines are marked on the central panel of Fig. 3 and one of them can be seen in panel 1 of Fig. 4, with two weak features in its wings on both sides of the line center that correspond to ν_2=1 $^{16}O_3$. These features are detected even if the spectrum suffers from small baseline ripples that could have masked them.

5.4. Carbon monoxide

CO J = 6–5 at 691473.000 MHz is also seen as a narrow line, confirming a vertical profile for this molecule quite different from those of O_3 and N_2O. The line can be seen in the zoom presented in panel 5 of Fig. 4. More specifically, the line profile appears to have a Gaussian component as expected for a mesospheric molecule. The CO abundance above 50 km has been

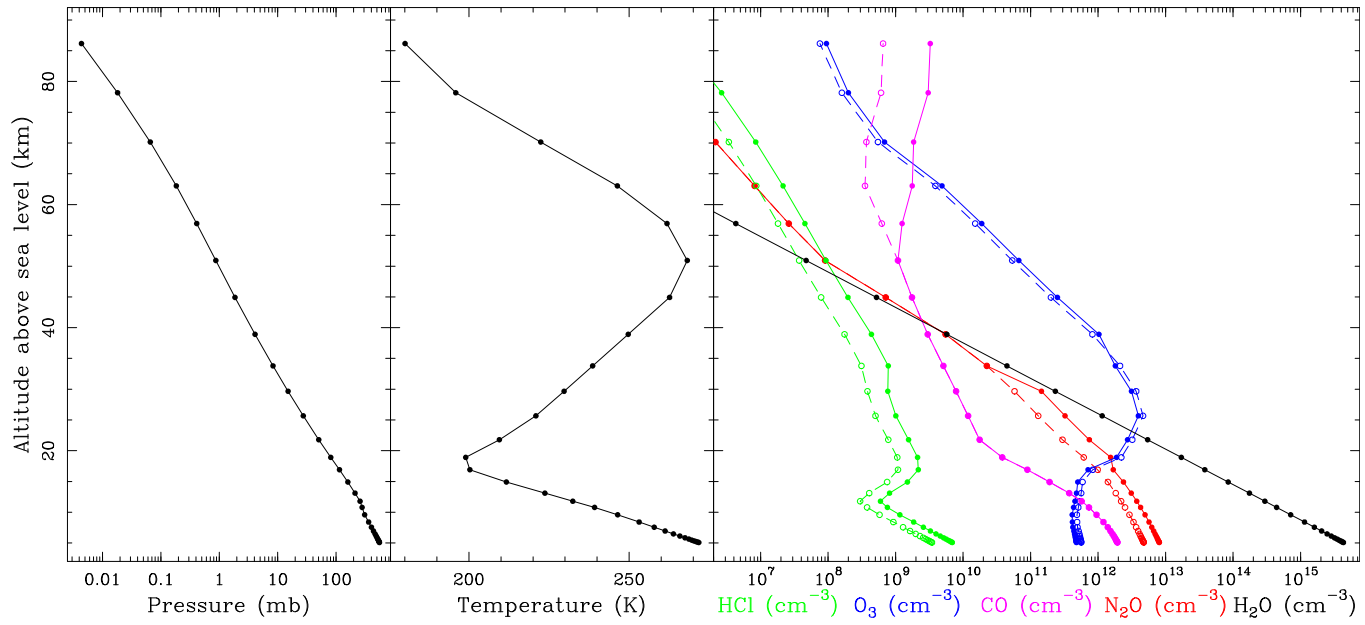

Fig. 5. Vertical profiles (solid lines) used as inputs to the ATM model for the model spectra shown in this work. The dots indicate the average values for the different layers (of increasing thickness) in which the atmosphere has been divided for the calculations. Dashed lines and open circles indicate profiles from U.S. Standard Atmosphere (COESA 1976) before being modified for a better fit to the observed lines of O_3, N_2O, HCl, and CO.

increased significantly in the model (see Fig. 5) to match the observed line profile.

There is another CO line within the observed frequency range, J = 5–4 at 576267.938 MHz. However, it is not detected because of the high opacity of H_2O in the troposphere resulting in a total absorption of any signal arriving from higher altitudes, where the narrow and Gaussian emission of CO originates.

5.5. Hydrogen chloride

HCl, an important gas in the chemistry of ozone depletion, is also detected through a triplet (see the inset in the second panel of Fig. 3), corresponding to the hyperfine structure of its J = 1–0 rotational transition, near 625.919 GHz. The signal from this triplet extends over ~100 MHz and reaches a main peak intensity of ~2 K above the wing of the 620.7 GHz H_2O line (at airmass = 1.0); see panel 2a of Fig. 4. From this observed signal, HCl has an abundance of over a factor of two larger than in the U.S. Standard Atmosphere (COESA 1976) which is possibly due to remaining chlorine pollution from the Chlorofluorocarbons (CFCs) era (see Fig. 5).

6. Model calculations and discussion

In this section, we present ATM model calculations – which include all species mentioned in the previous section – performed to be compared with the final re-calibrated data presented in the third panel of Fig. 3. We are not trying to fit the data using a single static atmospheric profile because, as already mentioned in Sect. 3, the atmospheric conditions were slightly changing during the observing run. On the other hand, the model calculations should make simple assumptions and rely upon a very limited number of parameters, with satisfactory results, for an operational code such as ATM. In particular, we adjusted the abundances and vertical distribution of some molecules (see Fig. 5) in order to get a reasonable match to their observed lines. The data allow some discrimination between different seasonal and/or day/night abundances and vertical distributions.

The model calculations shown in the third and fourth panels of Fig. 3 (red curves) were produced with the ATM code, varying only the ground temperature and the total PWVC every 1 GHz following the data from the log file plotted in the top panel of the same figure. The ground pressure was fixed to 555 hPa in accordance with the log file where this parameter appears almost constant, and the first-guess vertical profiles of p, T, and atmospheric gases come from the Tropical U.S. Standard Atmosphere (COESA 1976) for the site, which are pre-defined in the model, with small changes in the first few layers to match the ground values of p and T (the tropospheric lapse rate for the temperature has been adopted to be -5.6 K km^{-1}). The water vapor number density exponentially decreases with a scale height of 2.5 km. Based on the data themselves, the standard vertical profiles of O_3, N_2O, and CO have been changed at some altitudes to provide an overall satisfactory reproduction of all lines. Figure 5 shows the vertical profiles used in the calculations. Green dashed curves in Fig. 4 show the ATM model differences in $T_{\rm EBB}$ when using the vertical profiles from U.S. Standard Atmosphere (COESA 1976) with respect to the modified ones that provide a better fit to the data.

The use of the PWVC from the log file in the model calculations is justified by the good match between our PWVC retrieval described in Sect. 4.1 and the value in the log file, which comes from retrievals using the 183 GHz Water Vapor Radiometer. In any case, if the PWVC values from the log file were wrong or the model itself was inconsistent, then the forward calculations that we have performed would not match the data at all. This is not the case. In fact, very good agreement is obtained, within ~2% in the quadratic residual, smoothed over intervals of 1 GHz, $\overline{R}$, defined as:

$$\overline{R} = \sqrt{\frac{1}{N_{\rm airmasses}} \sum_{1}^{N_{\rm airmasses}} \left(\frac{\overline{T}_{\rm EBB,model} - \overline{T}_{\rm EBB,data}}{\overline{T}_{\rm EBB,data}} \right)^2}. \quad (3)$$

It is important to note that if there were a fundamental disagreement between data and model due to calibration issues or incorrect opacity terms, it would show up as airmass-dependent quadratic residuals. The fact that no such residuals are seen indicates:

1. The applied recalibration procedure is consistent. The recalibrated data, ATM model results, and reference atmospheric profiles used in the ATM calculations are available in electronic form at the CDS.

2. The empirical foreign wet CIA (H_2O-N_2 + H_2O-O_2) and dry CIA (N_2-N_2 + O_2-O_2 + N_2-O_2) that we are using (see Eqs. (30) and (31) in Pardo et al. 2001b, and the red, green and light-blue curves in the bottom panel of Fig. 3) are valid at least for the conditions of this experiment, which are similar to the conditions of the Mauna Kea experiment from which they were derived (Pardo et al. 2001a, 2005).

3. The self-wet CIA (H_2O–H_2O) is negligible for the very dry conditions of this experiment. ATM estimates this absorption to be almost two orders of magnitude lower than the foreign wet (H_2O–N_2 + H_2O–O_2) one at 664 GHz for 0.325 mm PWVC (0.00089 nepers of total opacity versus 0.06685 for airmass = 1.0).

In recent years, a number of publications have addressed the question of the non-resonant foreign wet and dry CIA in the atmosphere from theoretical calculations or laboratory experiments under tightly controlled conditions (Boissoles et al. 2003, Podobedov et al. 2008, Tretyakov at al. 2015, Serov et al. 2020). Our observations are under less controlled conditions and we detect the radiation after its propagation through the whole atmosphere to our detector. Therefore, we cannot address the fine details given in the above-cited publications. However, an empirical description of these opacity terms is obtained that works well for submm ground-based observatories.

It is also worth mentioning how well the different lines of the minor atmospheric gases are reproduced by the model, both in shape and intensity. Even the weakly detected features from O_3 isotopologs and vibrationally excited states are all reproduced relatively well by the model, as shown in Fig. 4. One aspect that remains to be checked is the possible seasonal or diurnal changes in those lines which is due to significant changes in the vertical distributions of the molecules responsible for them. Hopefully, new data of similar quality in the future will allow such studies.

7. Summary and conclusions

We obtained the first kilohertz-resolution atmospheric spectra in the 450 μm atmospheric window from a ground-based submm observatory. The conditions during the observations were relatively dry and stable. The performance of the receiver in terms of stability and sensitivity has produced data suitable for comparison with the atmospheric model currently implemented at ALMA, APEX, and other observatories, allowing us to check its overall validity, and also verify how well the weakest features of the atmospheric spectrum are reproduced.

The observations provide a very high level of spectral detail. The calibration offsets have been satisfactorily corrected, and the slowly varying atmospheric conditions are monitored and taken into account in the simulations. Very good agreement is obtained with the ATM simulations, proving that this model is adapted: no fundamental changes are necessary, for its use in the explored frequency range for astronomical sites located at ~5000 m above sea level. Only a few O_3 lines with high energy levels need small frequency corrections, and the vertical profiles of minor atmospheric gases have to be changed with respect to the standard a priori profiles currently used in the code. These changes will be implemented in the code for distribution. There is no evidence that the wet foreign and dry CIA empirical opacity terms need revision, at least under the conditions presented in this study. The better characterization of the ozone lines at this high resolution might be useful for a more accurate calibration (free from these features) of single-dish astronomical observations.

The next step in this study will be to explore the range ~157–510 GHz using data already obtained with the other APEX receivers under wetter and less stable conditions. The exploitation of those data will therefore be more complex and will be treated in a separate publication.

Acknowledgements. The APEX SEPIA receiver is a joint development by the Group of Advanced Receiver Development (GARD, Gothenburg, Sweden) from the Onsala Space Observatory (OSO, Sweden), the Netherlands Research School for Astronomy (NOVA, The Netherlands), and the European Southern Observatory (ESO). The authors thank ESO for funding this work through contract CFP/ESO/19/25417/HNE. JRP also thaks ESO for funding the implementation of ATM in the ALMA software under contract 14977/ESO/07/15694/YWE. JRP thanks Observatoire de Paris for supporting his work for this paper through its program "chercheurs invités" from Oct 10th to Dec. 10th 2021, and Ministerio de Ciencia e Innovación of Spain for funding support through projects PID2019-106110GB-I00, PID2019-107115GB-C21/AEI/10.13039/501100011033, PID2019-106235GB-I00. CP and JRP also acknowledge support from EUMETSAT under contract EUM/20/4600002477.

References

Belitsky, V., Lapkin, I., Fredrixon, M., et al. 2018, A&A, 612, A23
Boissoles, J., Boulet, C., Tipping, R. H., Brown, A., & Ma, Q. 2003, JQSRT, 82, 505
Chamberlin, R. A., Martin, R., Martin, C. L., & Stark, A. A. 2003, SPIE Proc., 4855, 609
COESA 1976, U.S. Standard Atmosphere, 1976 (Washington, DC: U.S. Government Printing Office)
Hesper, R., Khudchenko, A., Baryshev, A. M., Barkhof, J., & Mena, F. P. 2017, IEEE Trans. Terahertz Sci. Technol., 7, 686
Hills, R. E., Webster, A. S., Alston, D. A., et al. 1978, Infrared Phys., 18, 819
Klein, B., Hochgürtel, S., Krämer, I., et al. 2012, A&A, 542, A3
Klein, U., Loiselet, M., Mason, G., Gonzalez, R., & Brandt, M. 2016, ESA's Ice Cloud Imager on Metop Second Generation, EGU General Assembly Conference Abstracts, 17750
Matsushita, S., Matsuo, H., Pardo, J. R., & Radford S. 1999, PASJ, 51, 603
Mattioli, V., Accadia, Ch., Prigent, C., et al. 2019. Bull. Am. Meteorol. Soc., 100, 291
Mlawer, E. J., Turner, D. D., Paine, S. N., et al. 2019, JGR Atmos., 124, 8134
Paine, S., Blundell, R., Papa, D. C., Barrett, J. W., & Radford, S. J. E. 2000, PASP, 112, 108
Pardo, J. R., Serabyn, E., & Cernicharo, J. 2001a, JQSRT, 68, 419
Pardo, J. R., Cernicharo, J., & Serabyn, E. 2001b, IEEE Trans. Antennas Propag., 49, 12
Pardo, J. R., Serabyn, E., Wiedner, M. C., & Cernicharo, J. 2005, JQSRT, 96, 537
Pety, J. 2018, Submillimetre Single-dish Data Reduction and Array Combination Techniques, 11, 11
Podobedov, V. B., Plusquellic, D. F., Siegrist, K. E., et al. 2008. JQSRT, 109, 458
Polehampton, E., Hafok, H., & Muders, D. 2019, APEX Calibrator Manual, APEX Report APEX-MPI-MAN-0012, Rev. 1.3
Serov, E. A., Balashov, A. A., Tretyakov, M., et al. 2020, JQSRT, 242
Tretyakov, M. Yu., Sysoev, A. A., Odintsova, T. A., & Kyuberis, A. A. 2015, Radiophys. Quant. Electron., 58, 262
Ulich, B. L. 1980, ApJL, 21, 21
Ulich, B. L., & Haas, R. W. 1976, ApJS, 30, 247